Submitted to the Journal of Applied Physics,

Assigned manuscript # JR-9247

December 4, 2011

Drifting localization of ionization runaway: Unraveling the nature of anomalous transport in high power impulse magnetron sputtering

André Anders,* Pavel Ni, Albert Rauch

Lawrence Berkeley National Laboratory, Berkeley, California

*corresponding author: aanders@lbl.gov

ACKNOWLEDGMENT

We gratefully acknowledge the use of the gate and streak cameras offered by the Fusion Science and Ion Beam Technology Program. Technical support was provided by J. Wallig. A.R. thanks the Austrian Marshall Plan Foundation (www.marshallplan.at) for funding a scholarship. A.A. acknowledges support by the Assistant Secretary for Energy Efficiency and Renewable Energy, Office of Building Technology of the U.S. Department of Energy. This work was done at Lawrence Berkeley National Laboratory with support by the U.S. Department of Energy under Contract No. DE-AC02-05CH11231.

DISCLAIMER

This document was prepared as an account of work sponsored by the United States Government. While this document is believed to contain correct information, neither the United States Government nor any agency thereof, nor The Regents of the University of California, nor any of their employees, makes any warranty, express or implied, or assumes any legal responsibility for the accuracy, completeness, or usefulness of any information, apparatus, product, or process disclosed, or represents that its use would not infringe privately owned rights. Reference herein to any specific commercial product, process, or service by its trade name, trademark, manufacturer, or otherwise, does not necessarily constitute or imply its endorsement, recommendation, or favoring by the United States Government or any agency thereof, or The Regents of the University of California. The views and opinions of authors expressed herein do not necessarily state or reflect those of the United States Government or any agency thereof or The Regents of the University of California.

Drifting localization of ionization runaway: Unraveling the nature of anomalous transport in high power impulse magnetron sputtering

André Anders,* Pavel Ni, Albert Rauch

Lawrence Berkeley National Laboratory, Berkeley, California

Abstract

The plasma over the magnetron's erosion "racetrack" is not azimuthally uniform but concentrated in distinct dense plasma zones which move in the $\mathbf{E}\times\mathbf{B}$ direction with about 10% of the electrons' $\mathbf{E}\times\mathbf{B}/B^2$ drift velocity. The plasma zones are investigated with a gated camera working in concert with a streak camera for Al, Nb, Cu, and W targets in Ar or Kr background gas. It is found that each plasma zone has a high density edge which is the origin of a plasma-generating electron jet leaving the target zone. Each region of strong azimuthal density gradient generates an azimuthal electric field which promotes the escape of magnetized electrons and the formation of electron jets and plasma flares. The phenomena are proposed to be caused by an ionization instability where each dense plasma zone exhibits a high stopping power for drifting high energy electrons, thereby enhancing itself.

PACS numbers: 52.25.-b, 52.25.Jm, 52.35.Qz, 52.70.Kz, 52.80.Sm

*Corresponding author: aanders@lbl.gov

I. INTRODUCTION

Magnetron sputtering is a widely used physical vapor deposition technology. Its physics is reasonably well understood. To improve film quality for numerous applications, attempts have been made to ionize sputtered atoms, e.g. by adding a radio-frequency discharge[1] or by using very high magnetron power levels in a pulsed manner.[2] This contribution deals with the latter approach, often labeled as high power impulse magnetron sputtering (HIPIMS)[3-10] among other names.

The magnetron discharge is a magnetically enhanced glow discharge that can operate at very low background gas pressure (of order 1 Pa) due to confinement of the plasma electrons, and especially confinement of the energetic secondary electrons from the target. The specific magnetron geometry leads to a closed electron drift, where the main drift component is due to the $\mathbf{E}\times\mathbf{B}$ configuration, although $\nabla B\times\mathbf{B}$ and higher order drifts play a role too. The actual path of electrons is rather complicated: electrons gyrate around and move along the arched magnetic field lines and experience reflection from the sheath before reaching the target surface. The closed drift can be thought of a closed circular path over the racetrack when averaging over two sub-motions: (a) the electron gyration around magnetic field lines, giving the motion of the gyration center, and (b) the oscillation of the gyration center between reflection points at the sheath edge. The closed drift of electrons ensures that gas ionization can occur at low pressure because the complicated trajectory of electrons is constrained to the near-target region although the mean free path exceeds the characteristic length of the magnetron (e.g. the target radius) by a large factor.

For a magnetron discharge to work, a sufficient number of electrons needs to reach the anode, which is often a grounded shield placed outside the region of closed drift. It is well known that classical cross-field transport theory, where cross-field currents scale with B^{-2}, cannot explain the observed high discharge currents. Bohm introduced a semi-empirical cross-field diffusion coefficient leading to a current that scales with B^{-1}, ref.[11] Currents equal to or greater than the Bohm current are usually called "anomalous." Cross-field transport of the Bohm-type and greater are understood as being caused by collective phenomena such as plasma fluctuations and instabilities. The type of instability may depend on the specific geometry and collisional conditions. In this contribution we investigate plasma instabilities and put them in relation to the anomalous current found for magnetron discharges under HIPIMS conditions.[8,12,13]

HIPIMS discharges have previously been observed to show a range of waves and instabilities, which can be easily found, for example, in the traces of discharge current and voltage (for example, see Fig. 2 of ref.[14] or Fig. 1 of ref.[15], or Figs. 7-9 of ref.[3]). However, a most striking phenomenon of HIPIMS is the jump of the discharge current to a high level once a material and pressure dependent threshold voltage is reached or surpassed. This can be ascribed to a runaway of self-sputtering for high and medium sputter yield materials.[16] For low-yield materials, the high currents are related to a "gas recycling" mechanism which is analogous to the self-sputtering process.[17] For both self-sputtering and gas-based sputtering, neutral atoms are released from the target surface, ionized in the near-target region, and then accelerated back to the target by the pre-sheath and sheath electric field. Once returned to the target, the now energetic ions cause sputtering of surface atoms and the emission of secondary electrons. Should

the generation of neutrals and their ionization and return probabilities be high enough, the system can amplify (run away) until certain loss and dampening mechanisms terminate the runaway phase, leading to a sustained high current mode.[3]

The likelihood of a transition to an unwanted arcing mode is reduced by selecting relatively short (usually 100 μs or less) discharge pulses, where the pulse is terminated before the discharge current reaches its potential peak and/or goes into the above-mentioned high current phase. Short-pulse HIPIMS conditions are characterized, or can be defined by, a more-or-less triangular current $I(t)$ pulse shape, and many of the later-reported results were obtained under these conditions.

Focusing on the issue of cross-field current transport, Brenning and coworkers[12] reported on exceptionally high cross-field transport for $\mathbf{E}\times\mathbf{B}$ discharges where the power is abruptly enhanced: the cross diffusion coefficient was found to exceed the Bohm values by up to a factor 5. For the case of HIPIMS, the azimuthal electric current associated with the closed electron drift (Hall current) was experimentally found to be much smaller[14] than one would expect from earlier measurements using relatively low power direct current (dc) magnetrons,[18] or, in other words, the discharge current was unexpectedly larger than the Hall current. Lundin *et al.*[13] used electric field probe arrays to detect oscillating electric fields in the megahertz range. They interpreted their data by modified two-stream instabilities (MTSIs), which are known to promote transport of electrons across magnetic field lines.[19,20]

HIPIMS and mid-frequency magnetron discharges have been investigated with optical techniques. For example, Lopez and coworkers[21] used an intensified CCD camera to image the racetrack of a rectangular, mid-frequency pulsed magnetron (60 kHz, including a 3 μs reverse time) operating up to 1.5 kW. No information on time resolution and target size was provided, and there was no report on plasma instabilities, however, the plasma was found to be enhanced when the racetrack made sharp turns near the racetrack. Liebig and coworkers[22] used 2D-imaging in combination with Abel inversion to study the spatial and temporal evolution of the plasma-induced emission of aluminum and titanium HIPIMS discharges in argon (resolution 0.4 mm and 1 μs). They observed a significant development of the emission during the pulse on-time showing a structure similar to an ion acoustic wave travelling away from the target. Two maxima of neutral line emission was found using spectral filters indicating increased ionization of the sputtered metal flux as the pulse evolves. Recent imaging experiments at Bochum University showed that instabilities and periodic structures can be detected by a camera operated with a very short exposure time of 100 ns.[23]

The various pieces of information from probes, cameras, and spectrometers suggest that systematic optical measurements with high temporal and spatial resolution could provide much deeper insight into the type of instabilities causing anomalous current transport under HIPIMS conditions. Therefore, a combination of a gated camera and a streak camera is used in this contribution to obtain time-resolved images of HIPIMS discharges in end-on and side-on views. The report on optical data is complimented by some time-resolved emissive probe data giving information on the local plasma potential. We will show that azimuthally moving dense plasma structures exist that sometimes —but not always— appear in a regular, self-organized fashion. We will interpret the data as an azimuthal localization of the ionization runaway driven by energetic electrons, which are subject to $\mathbf{E}\times\mathbf{B}$ drift. We will further show that the formation of

an azimuthal electric field component gives rise to an axial velocity component of magnetically confined electrons. Finally we will relate the observation to instabilities observed in other $\mathbf{E}\times\mathbf{B}$ devices.

II. EXPERIMENTS

The experiments were done in a cylindrical stainless steel chamber of 35 cm inner diameter and 25 cm inner height. It was evacuated with a 550 l/s turbomolecular pump (Pfeiffer) backed by a diaphragm pump to a base pressure in the low 10^{-5} Pa range. High purity argon or krypton was injected using a mass flow controller (MKS). The flow rate could be adjusted up to 100 sccm to obtain the desired operational pressure, which was typically 0.3 Pa.

The HiPIMS discharge was powered by a HIPIMS high current pulse generator model SPIK2000A (Melec GmbH) capable of delivering pulses up to 1 kV, up to 500 A. Typical pulse lengths were 20-200 μs with a repetition rate of 100 or 200 pulses per second. The target current depends on the target material, gas type and gas pressure, and therefore actual pulse data are given below with each specific result. Additionally, the discharge is greatly affected by the magnetic field, and one can therefore observe shifts of current and other parameters as the target is gradually eroded – those changes, however, are not further investigated in this contribution.

The discharge current was recorded using a current transformer (Pearson model 101, sensitivity 0.01 V/A, bandwidth 0.25 Hz-4 MHz), and the discharge voltage was measured using a 100x voltage probe (Tektronix P5100). To impede fast high-amplitude oscillation that could damage the SPIK pulser, both output cables were wound three times through a ferrite ring before being connected to the target feedthrough (minus) and chamber ground (plus). All electrical signals were recorded with a National Instruments PXI-5105 high speed Digitizer/Oscilloscope with up to 60 MS/s real-time sampling rate per channel, operated under a LabView Signal Express program.

Figure 1 shows the experimental arrangement of the planar magnetron and two digital cameras for the end-on view experiment. For the side-on view, the camera setup was moved to the window located 90° from the one used in Fig. 1. Each window had a movable shutter that was opened only when taking images to minimize buildup of a coating on the window. The cameras were used simultaneously using a 50/50 optical beam splitter, a semi-transparently coated flat glass, as indicated in Fig 1.

The gated camera (Princeton Instruments PIMAX 1024) was equipped with a f = 80 mm Nikon lens and a micro-channel plate (MCP) amplifier delivering 512 pixels × 512 pixels images with 16 bit greyscale intensity resolution. The exposure time was varied down to 1 ns. The camera uses light emitted from the plasma in the visible part of the spectrum, with the greatest quantum efficiency in the blue part of the spectrum.

The streak camera was a Hamamatsu C7700 with a f = 35 mm Nikon lens and detector model C4742-98. It produces images where the horizontal direction is a spatial dimension (x for end-on view, and z for side-on view), and the vertical direction is time. The image dimensions were 1344 pixel in space and 1024 pixel for the time axis, with 14 bit intensity resolution. The slit width was no wider than 10 pixels. Electronic image amplification was kept low to always

stay well below the saturation of the detectors. The amplification factor was not kept constant but adjusted to the specific conditions in order to obtain a reasonable dynamic range of the image; this needs to be taken into account when comparing images taken under different conditions. The images were loaded into a computer and digitally flipped and rotated as needed, to present the magnetron in such orientation as one would see it through the vacuum chamber window. The false color scale "royal" of the image processing software *ImageJ*[24] was applied to enhance the visual presentation of the images.

The side-on view presents a slightly greater challenge than the end-on views since one essentially looks at two regions of plasma: one over the target erosion zone ("racetrack") close to the camera, and the other over the racetrack zone behind it. Both cannot be imaged in focus due the limited field-of-depth (a few millimeters). Even if the field-of-depth was not an issue, the presence of two plasma zones would make interpretation of images difficult. Therefore, to block the view to the more remote plasma region, a long, 1.5 mm diameter alumina ceramic rod was carefully positioned on axis. As a result, the streak camera in side-on view recorded only the plasma that is on the left as seen from the end-on window, i.e. position $\left(x = 22\,\text{mm},\, y = 0,\, z \parallel \text{slit}\right)$. We note that the ceramic rod on the center axis of the discharge system did not affect the electrical properties of the discharge when the ceramic was installed.

The planar magnetron was operated with a 6.25 mm (1/4") thick, 76 mm (3") diameter target of Al, Cu, Nb, or W. The selection of targets and gases was made to investigate whether or not the instabilities depend on target material and/or gas type. The magnetron was of the "keeper type" (US Inc., now Meivac Inc.): the target is kept in place with the help of the magnetic field that also provides the magnetron structure for the discharge. This works as follows: a 25 mm diameter, 1 mm thick steel disk is screwed in the center of the backside of the target; this steel disk, and with it the whole target, is magnetically clamped to the central magnet of the magnetron. No mechanical clamp ring is needed. The anode is a grounded annual metal ring whose one end is mounted flush with the target surface. Magnetic target mount and flush anode allowed us to have unimpeded view at the target surface in both end-on and side-on views, which is not the case with the more-common clamp-style magnetrons.

The magnetic field structure of this magnetron was mapped using a small Hall probe (F.W. Bell 5180 Gaussmeter) that was automatically moved to many positions using a stepper motor. Both axial and radial components were recorded, and a field map was constructed (Fig 2) showing that this magnetic is unbalanced.

In a separate experiment with pulsed emissive probes, which will be described in detail in a separate publication,[25] the local plasma potential was recorded as a function of time. For various axial (z) positions, the probe was automatically moved in radial (r) direction and the probe signals were recorded with the National Instruments PXI-5105 data acquisition system. The pre-target region was mapped with the exception of the plasma region near the racetrack. This region had to be excluded since the disturbance by the probe was severe. In extreme cases, the probe caused the magnetron discharge to cease.

All system components (discharge, gated and streak cameras, and probe data acquisition) were synchronized through a common pulse generator (the experiment's "clock") and delay/pulse generators as indicated in Fig. 1.

III. RESULTS

A first experimental series, in which the gated camera was used with different exposure times, revealed the presence of significant azimuthal plasma non-uniformities. While relatively long gate times in the microsecond range showed the familiar plasma ring over the target erosion zone (the "racetrack"), very distinct features became visible when using a gate time of 1 μs or shorter, as demonstrated by the series of images shown in Fig. 3 (the "gate time" of a digital camera is fully equivalent to the "exposure time" known from conventional photography, and we use those terms synonymously). Our experiments included even longer (up to 50 μs) and shorter (down to 1 ns) gate times but they revealed no additional information. They are therefore not further shown or discussed. From the set of images of Fig. 3 one can draw first conclusions, namely (a) the visual appearance of a plasma ring is the result of azimuthal motion of dense plasma zones, (b) the time needed for one rotation is about 15 μs (the corresponding rotation frequency is ~ 60-80 kHz); using the circumference of the racetrack of about 150 mm, the related velocity is about 10^4 m/s, (c) the structures appear clearly once the exposure time was reduced to about 100 ns. Further reduction did not reveal additional information but increased the noise in the images. We opted using 10 ns gate time for the remainder of the work as a compromise between image noise and avoiding blurring by motion of plasma structures.

Hundreds of 10 ns images were taken for different conditions. One of them is shown in Fig. 4 (top) combined with a streak image of the same pulse (bottom). One can clearly identify 4 distinct zones of high density, which were labeled A, B, C, and D. In this particular example, the spacing between the zones is about equal. Many, but not all, of the images show signs of equal spacing, pattering, or self-organization. The streak images unequivocally reveal that all of the dense zones move azimuthally with about the same speed in the counterclockwise direction, i.e. the same direction of the electrons' $\mathbf{E}\times\mathbf{B}$ drift.

The specific velocity depends on both the gas type and target material. We have tested Ar and Kr gas for Al, Cu, Nb, and W targets. The result is shown in Table I, where the plus-minus values are not measurement error bars but a range of velocities observed in several ten measurements per material combination.

Table I. Velocity of the counterclockwise, azimuthal motion of dense plasma zones observed for different gas and target material combinations. The measurement error is in the range ±50 m/s, and the given intervals refer to variations seen in the observation of several 10 measurements per gas-target combination. Atomic mass and the approximate target surface binding energies or sublimation energies (which affect the sputter yields) are also provided.[26]

The plasma pattern tends to evolve and change during a pulse. For example, one can see the appearance of an additional dense plasma zone in the right lower corner of the streak image (Fig. 4) just before the end of the discharge pulse.

Figure 5 shows an example of a plasma structure that is not very regular (as opposed to the regular pattern shown in Fig. 4). The top part of Fig. 5 shows the end-on gated image, while

the bottom shows the corresponding side-on streak image with the discharge current pulse laid over it. The streak image shows distinct jets of electrons emitted from the dense plasma zone as is evident by the propagating excitation and light emission caused by the emitted electrons. The tilt of the jets (with one dimension in space, *z*, and the other in time, *t*) let us determine the velocity propagation from the target, namely about 2×10^4 m/s. The ejection of electrons from the dense plasma is perhaps the most striking evince of the role of instabilities and self-organized patterns for the cross-field transport of electrons. The correlation of dense plasma structures and electron jets is evident in the four other examples of side-on streak images shown in Fig. 6. The slope of the bright jets in the (*z*,*t*) plane indicates that all have approximately the same velocity, although there are variations. It is apparent that the velocity of the electron jets increases as the discharge pulse evolves and the current, power, and plasma density increase.

In a next step, both gated and streak cameras observed the plasma in side-on view. Fig. 7 shows an example, where the gated image (Fig. 7 top) was taken right at the peak of the discharge current. We see that the electron jet causes a plasma flare in the center of the upper image. The flare is tilted with respect to the *z*-axis; it trails the dense plasma zone which is moving down in this presentation.

The detailed optical investigations were supplemented with probe measurements, most of which will be reported in a separate publication.[25] Here we only include a couple of complementary measurements to show the direct relation between optical and probe data. The emissive probe measurements were designed to determine the local, time-dependent plasma potential. Fig. 8 shows two examples of measurements, one almost over the racetrack at r = 28 mm but at a distance of z = 16 mm away from the target surface, and the other very close to the surface, at z = 1 mm, but outside at r = 36 mm, which is 14 mm from the racetrack center. As the plasma forms, the potential shifts to negative values with respect to ground, and exhibits more or less regular fluctuations which have about the same frequency as the appearance of dense plasma at a given location over the racetrack.

IV. DISCUSSION

It is well established that dense plasma forms in HIPIMS processes by ionization of the neutrals which are largely supplied from the target surface: either surface atoms that were sputtered or former gas ions that were neutralized at the target.[17] The literature on HIPIMS generally does not specify anything about the localization of ionization processes other than that ionization processes are concentrated in the near-target zone, i.e. the magnetic pre-sheath, which is determined by the arched magnetic field. Fig. 3 shows that ionization processes and the plasma density are not azimuthally uniform but concentrated in dense plasma zones, which may be called ionization zones, or rotating spokes, in analogy to the rotating spoke instability known from Hall thrusters.[27]

Ionization by electron impact is known to be the main mechanisms for plasma production in low-pressure magnetron discharges. The energetic electrons needed for the process stem from secondary electrons emitted from the target by primary ion impact and photo emission processes. The emitted electrons become energetic electrons by acceleration when they cross the electric field of the sheath and pre-sheath. As mentioned in the Introduction, the actual trajectory of

electrons is rather complicated due to the magnetization in the non-uniform magnetic field. "Magnetization" implies that the electron gyration radius

$$r_{g,e} = \frac{u_{e\perp}}{\omega_e} = \frac{m_e u_{e\perp}}{eB}. \tag{1}$$

is small compared to the thickness of the sheath-pre-sheath region, otherwise the electrons would not be well confined and one could not find structures related to the field lines. In Eq. (1), $u_{e\perp}$ is the velocity component perpendicular to the magnetic inductance vector $\mathbf{B}$, and $\omega_e = eB/m_e$ is the electron cyclotron frequency. The gyration center of magnetized electrons follows magnetic field lines in the absence of an electric field, but a drift occurs when an additional force acts on the electrons, most importantly the force caused by the pre-sheath's electric field. The $\mathbf{E}$ vector is pointing toward the target surface and $\mathbf{B}$ has a transverse (radial) direction to the center of the target when the magnetic field arches over the racetrack region. This results in an azimuthal electron drift velocity according to[11]

$$\mathbf{v}_{Hall} = \mathbf{E} \times \mathbf{B} / B^2 \tag{2}$$

which is in counterclockwise direction if the target is seen from the camera position. The approximate electron drift velocity over the racetrack can be readily estimated using the magnetic field $B \sim 100$ mT (*cf.* Fig. 2) in conjunction with the electric field determined by an emissive probe ($E \sim 10^4$ V/m, ref.[25]), leading to $v_{\mathrm{Hall}} \sim 10^5$ m/s, in agreement with estimates by others.[28]

The ion gyration radius is much larger than the characteristic length of the target zone, and hence ion motion is mainly determined by the local electric field. The same electric field that is used to determine the $\mathbf{E} \times \mathbf{B}$ drift accelerates practically all ions formed in the pre-sheath to the target where they cause sputtering and emission of secondary electrons.

Depending on the emission conditions, and especially on the tilt of the local magnetic field relative to the target surface, secondary electrons are either immediately recaptured by the target[29] or they can escape. Escaping electrons pick up substantial kinetic energy (corresponding to about 90% of the applied voltage) as they cross the sheath.

The key to understanding ionization processes is to follow the paths of energetic electrons as they gyrate around the arched magnetic field lines while moving back and forth between reflection points and, in the average, drift perpendicularly to both **E** and **B**. The electron mean free path between collisions is determined by the densities of all kinds of particles the electron can interact with, n_p, and the velocity-dependent interaction cross sections, $\sigma_{ep}(v)$, where we have to sum over all types of particles *p* present in the plasma:

$$\lambda_e^{-1} = \sum_p \sigma_{ep} n_p. \tag{3}$$

Both elastic and inelastic collisions contribute to transfer of energy from fast secondary electrons to other plasma particles. The cross sections vary greatly depending on the materials and relative velocity upon impact. They are very well investigated for the case of electrons interacting with

argon atoms. In the interesting range of about 500 eV, the elastic collision cross section is greater than the cross sections for electron impact ionization and excitation[30] (Fig. 9).

Fast electrons not only interact with atoms but also experience Coulomb interactions with ions and electrons and transfer their energy to them. Spitzer[31] derived a formula for the characteristic thermalization time for fast charged particles moving in a background of charged slow "field particles" (index *f*). In our case the fast particles are the energetic secondary electrons and the slow particles are singly charged ions (index *i*) and thermal (Maxwell-distributed) electrons (index *e*):

$$t_{therm,(e-f)} = \frac{4\pi\varepsilon_0^2 m_e^2 v_{se}^3}{e^4\left(1+m_e/m_f\right)n_f \ln\Lambda} \tag{4}$$

where $\varepsilon_0 = 8.854\times10^{-12}\,\mathrm{As/Vm}$ is the permittivity of free space, v_{se} is the velocity of fast electrons before slowing down, and $\ln\Lambda \approx 10$ is the Coulomb logarithm. Since the interaction is with both ions and background electrons, and using the quasi-neutral condition of the magnetic pre-sheath $n_e \approx n_i$, one can write

$$t_{therm}^{-1} = t_{therm,(e-e)}^{-1} + t_{therm,(e-i)}^{-1} = \frac{e^4 n_e \ln\Lambda}{2\pi\varepsilon_0^2 m_e^2 v_{se}^3} + \frac{e^4 n_i \ln\Lambda}{4\pi\varepsilon_0^2 m_e^2 v_{se}^3} = \frac{3e^4 \ln\Lambda}{4\pi\varepsilon_0^2 m_e^2}\frac{n_e}{v_{se}^3} \tag{5}$$

The resulting estimate for the thermalization time is shown in Fig. 10. We see that secondary electrons, after they have gained several 100 eV by acceleration in the sheath, do not slow down much as long as the plasma is of low density (e.g. 10^{16} m^{-3}). In this region of the energy-density space, it is much more likely that inelastic collisions with neutrals lead to a slow down. The total cross section is about $\sigma_{e-Ar} \approx 3\times10^{-20}\,\mathrm{m}^2$ (see Fig. 9); the argon density at an argon partial pressure of $p_{Ar} = 0.5\,\mathrm{Pa}$ is about $n_{Ar} = p_{Ar}/kT_{Ar} \approx 7\times10^{19}\,\mathrm{m}^{-3}$, resulting in $\lambda_{e-Ar} \approx 0.5\,\mathrm{m}$. Fast electrons travel with $v_{se} \approx 10^7\,\mathrm{m/s}$, giving a characteristic time to a collision $t_{e-Ar} = \lambda_{e-Ar}/v_{se} \approx 50\,\mathrm{ns}$, which is much shorter than the thermalization time for energetic electrons (Fig. 10).

This leads us to consider the following mechanism for the ionization instability and the formation of zones of dense plasma. Suppose there is a fluctuation δn_{Ar} of the neutral gas density around the average value n_{Ar0}, then the actual value of the neutral density can be written as

$$n_{Ar} = n_{Ar0} + \delta n_{Ar}\,. \tag{6}$$

At the beginning of the process, secondary electrons drifting in the $\mathbf{E}\times\mathbf{B}$ field have a mean free path

$$\lambda_e^{-1} = \sum_p \sigma_{ep} n_p \approx \sigma_{e-Ar} n_{Ar} \tag{7}$$

which becomes shorter by $\delta\lambda_e^{-1} = \sigma_{e-Ar}\delta n_{Ar}$ due to the presence of the fluctuation, and hence the probability of an interaction is somewhat greater at the location of the fluctuation. Statistically, energetic electrons produce more ions at the location of the fluctuation. The balance equation reads

$$\frac{\partial n_i}{\partial t} = K_\alpha n_{Ar} n_e - K_\beta n_e^2 n_i - \nabla\left(n_i \mathbf{v}_i\right), \tag{8}$$

where K_α and K_β are the ionization and recombination rate coefficients, and the last term describes the plasma flow due to diffusion and drift (the index *i* refers here to argon ions but later in the process atoms and ions of the target material play a role too). The ionization and recombination coefficients are[32,33]

$$K_\alpha = \int f_e\left(E\right) E^{1/2}\, \sigma_{e-Ar}\left(E\right) dE \tag{9}$$

$$K_\beta \approx \frac{4}{9}\left(\frac{2\pi}{m_e}\right)^{1/2}\left(\frac{e^2}{4\pi\,\varepsilon_0}\right)^5 \left(kT_e\right)^{-9/2}. \tag{10}$$

where E is the electron energy, and $f_e\left(E\right)$ is the electron energy distribution function. A positive fluctuation of the gas density leads to more ionization, which can be expressed as

$$\left(\partial n_i/\partial t\right)_{ionization} = K_\alpha\left(n_{Ar0} + \delta n_{Ar}\right)\left(n_e + \delta n_e\right). \tag{11}$$

A strong positive feedback between density and shortening of the mean free path can develop by the synergy of several factors. First, ionizing collisions create a higher plasma density, which increases the Coulomb interaction between fast electrons and background ions and electrons. The slowing of the fast electrons heats the background electrons, i.e. the energetic tail of the thermalized part of the electron energy distribution function energy is enhanced. This in turn promotes more ionization. The slowed-down fast electrons, still more energetic than the thermalized population, experience even greater slowing in the denser plasma region as shown in Fig. 10. Second, when an energetic electron of some 100 eV loses energy in a collision, it is more likely to cause more excitation, ionization, and elastic collisions due to the energy-dependence of the cross sections in Fig. 9. In other words, the ionization rate (11) is enhanced due to increase in the free electron density as well as due to a change of the electron distribution function affecting the coefficient K_α. Third, electrons produced in ionizing collisions have much less energy than the energetic electron causing the ionization (for example half or less than half of the energy of the impacting electron, see e.g. ref.[34,35]). Considering the energy-dependence of the ionization cross section, lower energy electrons have a much shorter mean free path and greater probability of causing ionization until they are on the low-energy side of the maximum of the ionization cross section. While detailed simulation is needed to capture all those interdependencies, it is safe to say that there is a highly non-linear feedback and a reduction of the mean free path when energetic electrons encounter a region of initially higher neutral density. The non-linear feedback will turn the fluctuation of neutral density into a region of higher plasma density.

In a next step we consider what happens to the newly produced ions and electrons. An electric field is present in the magnetic pre-sheath and causes electrons to drift ($\mathbf{E}\times\mathbf{B}$ and higher order drifts) and ions to move toward to the sheath edge, where they are further accelerated to the target surface. Surface atoms are sputtered and secondary electrons are emitted. That means that the local enhancement of the plasma density is followed by an increased local production of neutrals, namely the sputtered atoms and neutralized gas (the former gas ions). The enhanced supply of neutrals brings the opportunity to locally even further enhance the plasma density: this was previously discussed as runaway of self-sputtering and near-target gas trapping.[17]

The location of highest ionization probability depends on both the density of energetic electrons and density of neutral atoms to be ionized, as expressed in the ionization term of Eq. (8). The position of highest plasma density is not fixed because the electrons are subject to the $\mathbf{E}\times\mathbf{B}$ and higher order drifts, which shift the location of greatest stopping power (a term liberally borrowed from the field of particle-solid interactions). If this were the only factor one would expect that the azimuthal motion of a dense plasma zone is in the $\mathbf{E}\times\mathbf{B}$ direction with the drift speed according to equation (2). We do observe the plasma moving in the $\mathbf{E}\times\mathbf{B}$ direction but only with about 10% of the electron drift speed. It is conceivable that the formation of dense plasma locally changes the E and B fields. For example, probe measurements[25] indicate a redistribution of the plasma potential, pushing more of the voltage drop closer to the target. This could result in a slow-down of the azimuthal drift in the pre-sheath. Additionally, and perhaps more importantly, the availability of neutrals affects the plasma production and resulting azimuthal speed. Neutrals are provided by the background gas and the target, however only fluxes from the surface can explain the magnitude of discharge currents observed in HIPIMS discharges.[17] The speed of the azimuthal motion of a dense plasma zone is affected by the inertia of ions to the target and atoms from the target, as expressed by an ion-atom-ion cycle or "recycle" time, $t_{rec} = t_i + t_a$, with

$$t_i \approx \sqrt{\frac{2d}{E}\frac{m_i}{e}}\,, \tag{12}$$

$$t_a = d/v_a\,, \tag{13}$$

where d is a characteristic distance between ionization location and the target surface, and v_a is a typical velocity of atoms moving from the surface. The evaluation of those expressions is complicated since the field E is not constant and v_a depends on whether the atom was sputtered, reflected, or outgassed. For the purpose of an order-of-magnitude estimate we take niobium (mass 93), $d \approx 10^{-3}\,\mathrm{m}$, $E > 10^4\,\mathrm{V/m}$, $v_a > 2\times10^3\,\mathrm{m/s}$, and obtain $t_i < 0.4\,\mu\mathrm{s}$ and $t_a < 0.5\,\mu\mathrm{s}$. The effect of material inertia can be seen in the data of Table I. With the exception of copper, the azimuthal motion of dense plasma with krypton (mass 84) is slower than the motion when using argon (mass 40). Comparing different target materials one sees the same trend: heavier target materials exhibit a slower azimuthal motion. The insensitivity of copper to the type of gas can readily be explained by the large self-sputter yield of copper: it is well known that high yield materials such as copper displace the process gas and essentially operate in a "gas" of the target material.[36-38] Aluminum has a surface binding energy comparable to copper but the

displacement of gas is much weaker due to the light mass of aluminum compared to argon or krypton.

The proposed ionization amplification associated with the stopping of energetic electrons is consistent with the peculiar triangular shape of the dense zone keeping in mind that the actual trajectory of magnetized electrons is essentially along the magnetic field lines. As mentioned before, electrons gyrate around the arched magnetic field lines and the gyration center of an electron oscillates between points on both sides of the racetrack; the azimuthal $\mathbf{E}\times\mathbf{B}$ drift is just a net motion of the gyration center. The oscillating part of the motion is approximately perpendicular to the drift. The ionization instability evolves within a mean free path according to Eq. (3) which must be compared to the azimuthal drift length between ionizing collisions. If the azimuthal length is short, we can expect to observe a sharply defined plasma density evolving along the arched field lines, e.g. perpendicular to the azimuthal drift (Fig. 11). The bright plasma zone tapers off in the direction of the drift as the energy of energetic electrons is exhausted after many collisions. Interestingly, a very similar triangular-like zone of tapering-off excitation and dense plasma has been observed when an arc spot supplies copious amounts of electrons to the magnetron configuration (*cf*. Fig. 3 of ref.[39]).

We can identify the plasma plume behind the sharp plasma boundary in Fig. 11 as a trailing plasma flare consistent with the observations of electron jets originating from the dense plasma zone shown in Figs. 6 and 7. Another example of such trailing plasma can be seen in Fig. 5, top, at about (x = 22 mm, y = 0). The formation of one or more dense plasma zones has thus interesting implications for the current transport. The $\mathbf{E}\times\mathbf{B}$ drift gives rise to the Hall current $\mathbf{j}_{Hall} = -en_e\mathbf{v}_{Hall}$ where the minus sign is due to the negative charge of electrons and $\mathbf{v}_{Hall}$ was introduced by Eq. (2). In a first approximation we assume that the electron drift leading to a Hall current is purely azimuthal, $|\mathbf{j}_{Hall}| = |j_\theta| = env_{e\theta}$, where θ is the azimuthal angle and $v_{e\theta}$ is the azimuthal drift velocity of electrons. Then the associated continuity and momentum equations are

$$\frac{\partial}{\partial\theta}\left(n_e v_{e\theta}\right) = 0 \tag{14}$$

$$m_e v_{e\theta}\frac{\partial v_{e\theta}}{\partial\theta} = -eE_\theta\,, \tag{15}$$

where E_θ is an azimuthal electric field. From Eq. (14) we can see that when the Hall current encounters a higher density zone, the azimuthal electron velocity cannot be constant, rather, it needs to be reduced. Equation (15) tells us that an azimuthal electric field must exist when the azimuthal electron velocity is reduced. Such azimuthal electric field would generate a new electron drift according to

$$\mathbf{v}_z = \mathbf{E}_\theta\times\mathbf{B}/B^2 \tag{16}$$

which points away from the target since $\mathbf{B}$ is a radial field over the racetrack pointing to the center of the target. In case of a reversed magnetic field, with the $\mathbf{B}$ vector pointing away from the target center, the azimuthal drift motion of electrons and plasma zones is clockwise. The

azimuthal field vector $\mathbf{E}_\theta$ would be reversed, and thus the resulting electron jets point away from the target in that case, too. Hence, the polarity of the magnetic field does not matter for the direction of the electron jets.

These arguments suggest that the formation of a dense plasma zone is necessarily related to the generation of a plasma flare caused by the energetic electrons leaving the confinement region. The greatest axial electron flow should be expected where $\partial n_e / \partial \theta$ is greatest, i.e. where we see the sharpest azimuthal gradient in the plasma. The plasma is much wider there (in the radial direction, see Fig. 11), leading to a broadening of the erosion track and the often-mentioned better target utilization when using HIPIMS,[2,10] compared to target utilization by direct current (dc) and radio-frequency (rf) sputtering.

Potential measurements by the emissive probe allow us to estimate the azimuthal electric field. From Fig. 8 we see that the plasma potential varies by about 5 V as the dense plasma zone passes the stationary emissive probe. Since the probe was kept away from the dense plasma in order to minimize disturbing it, it seems safe to assume that the potential variations closer to the target are of the order 10 V or greater. The length scale of such change is 10^{-2} m or less, resulting in $E_\theta > 10^3\,\mathrm{V/m}$. Inserting this in Eq. (16) and using $B_r = 0.1\,\mathrm{T}$ gives $v_z > 10^4\,\mathrm{m/s}$. This velocity is somewhat faster than the observed azimuthal speed of the dense plasma zones, and therefore an electron jet or plasma flare emitted from the edge of a dense plasma zone is likely to be visible from the side as being tilted in about the range 10°-45° with respect to the *z*-axis. The flare shown in Fig. 7 (top) appears to be emitted from the dense plasma at $y \approx -6\,\mathrm{mm}$, trailing the dense plasma which moves down in the direction of negative *y*, which is consistent with a counterclockwise azimuthal motion. The flare's apparent angle is about 30° with respect to the *z*-axis.

The absolute speed of the electron jets (generating the plasma flares) was determined using side-on streak images such as those in Fig. 6 and Fig. 7 (bottom). For example, the central bright flare in Fig. 7 (bottom) indicates $v_z \approx 2\,\mathrm{cm}/1\,\mu\mathrm{s} = 2\times10^4\,\mathrm{m/s}$, well within the previous estimate from the gated camera. However, the jet emitted from the dense plasma zone at 39 μs is about two times faster than the others.

The streak images in Fig. 6 further indicate that the velocity of electron jets is smaller at the beginning of the pulse when the current and plasma density are still low. One can also see that some jets seem to slow down as the distance to the target increases. The concept of the jets being driven by $\mathbf{E}_\theta \times \mathbf{B}/B^2$ is subject to further investigation: the velocity scales with $|E/B|$ where both the electric field and the magnetic field decrease with increasing distance from the target surface. While the correlation of azimuthal plasma density gradients and jet generation is firmly established by images such as those in Figs. 6 and 7, the electron propagation and plasma generation need to be modeled taking azimuthal and axial drifts and instabilities into account.

At the end of this discussion we step back and compare the results with plasma behavior in other $\mathbf{E}\times\mathbf{B}$ configurations. The perhaps most studied are Hall thrusters which were introduced decades ago and recently gained renewed and increased interest.[27,40-46] At least seven different modes and types of instabilities have been identified, all operating in different, sometimes overlapping ranges of frequency. Some are in the 10-100 kHz range and have other

similarities; among them are the *breathing mode*, *rotating spoke mode*, and azimuthal *drift magnetosonic waves*[27,47-50]. Slow instabilities have also been found in the output current of plasma guides (macroparticle filters) for vacuum arc plasmas (*cf*. Fig. 13 of ref.[51]) and in hollow cathode discharges with axial magnetic field.[52,53] The point of this long list of references is that plasma instabilities under $\mathbf{E}\times\mathbf{B}$ conditions are the rule, not the exception, and one should not be surprised that HIPIMS discharges contribute to this rich field.

V. SUMMARY

High power impulse magnetron sputtering (HIPIMS) is one form of an $\mathbf{E}\times\mathbf{B}$ discharge with the specific feature that a large fraction of the to-be-ionized neutrals are supplied by the target. As most other $\mathbf{E}\times\mathbf{B}$ discharges, HIPIMS exhibits instabilities that are essential in providing the physical, non-classical mechanism for electron transport across magnetic field lines. By simultaneously using gated and streak cameras it was firmly established that the plasma is concentrated in dense plasma zones that travel azimuthally in the same direction as the electrons' $\mathbf{E}\times\mathbf{B}$ drift, although much slower than the $\mathbf{E}\times\mathbf{B}/B^2$ velocity. It is argued that each of the dense plasma zones is associated with an azimuthal electric field, which breaks the magnetic confinement of electrons via a $\mathbf{E}_\theta\times\mathbf{B}/B^2$ drift component, which is in the axial direction, i.e. away from the target. The formation of electron jets and plasma flares is clearly visible in side-on gated and streak images, with the root or origin clearly related to the location of greatest azimuthal gradient of the dense plasma zones. Since the azimuthal velocity of the dense plasma is less than the electrons' $\mathbf{E}\times\mathbf{B}/B^2$ drift, it has been proposed that the dense plasma zone has a high stopping power (i.e. greatly reduced mean path) for the drifting energetic electrons, which in turns leads to an enhancement of the dense plasma itself. Therefore, plasma fluctuations tend to grow at the expense of less ionization events downstream. As a result, a dense plasma zone assumes a triangular shape, with the densest part along a magnetic field line, which is perpendicular to the azimuthal drift. The often observed widening of the erosion track of a target under HIPIMS conditions, leading to better target utilization, is clearly associated with the width of the dense plasma forming and amplifying around this magnetic field line.

While the relation of azimuthally non-uniform plasma zones and the formation of electron jets and plasma flares is clearly established, the need for detailed modeling is greater than ever. It is assumed that the measurements and the interpretation presented here can guide future modeling.

ACKNOWLEDGMENTS

We gratefully acknowledge the use of the gate and streak cameras offered by the Fusion Science and Ion Beam Technology Program. Technical support was provided by J. Wallig. A.R. thanks the Austrian Marshall Plan Foundation (www.marshallplan.at) for funding a scholarship. A.A. acknowledges support by the Assistant Secretary for Energy Efficiency and Renewable Energy, Office of Building Technology of the U.S. Department of Energy. This work was done at

Lawrence Berkeley National Laboratory with support by the U.S. Department of Energy under Contract No. DE-AC02-05CH11231.

References

[1] J. Hopwood, Phys. Plasmas **5,** 1624 (1998).
[2] V. Kouznetsov, K. Macak, J. M. Schneider, U. Helmersson, and I. Petrov, Surf. Coat. Technol. **122,** 290 (1999).
[3] A. Anders, Surf. Coat. Technol. **205,** S1 (2011).
[4] A. Ehiasarian, in *Plasma Surface Engineering Research and its Practical Applications*, edited by R. Wei (Research Signpost, Kerala, India, 2008), p. 35.
[5] G. Clarke, A. Mishra, P. J. Kelly, and J. W. Bradley, Plasma Processes and Polymers **6,** S548 (2009).
[6] J. T. Gudmundsson, P. Sigurjonsson, P. Larsson, D. Lundin, and U. Helmersson, J. Appl. Phys. **105,** 123302 (2009).
[7] U. Helmersson, M. Lattemann, J. Bohlmark, A. P. Ehiasarian, and J. T. Gudmundsson, Thin Solid Films **513,** 1 (2006).
[8] D. Lundin, P. Larsson, E. Wallin, M. Lattemann, N. Brenning, and U. Helmersson, Plasma Sources Sci. Technol. **17,** 035021 (2008).
[9] D. Lundin, S. A. Sahab, N. Brenning, C. Huo, and U. Helmersson, Plasma Sources Sci. Technol. **20,** 045003 (2011).
[10] K. Sarakinos, J. Alami, and S. Konstantinidis, Surf. Coat. Technol. **204,** 1661 (2010).
[11] F. F. Chen, *Plasma Physics and Controlled Fusion* (Plenum Press, New York, 1984).
[12] N. Brenning, R. L. Merlino, D. Lundin, M. A. Raadu, and U. Helmersson, Phys. Rev. Lett. **103,** 225003 (2009).
[13] D. Lundin, U. Helmersson, S. Kirkpatrick, S. Rohde, and N. Brenning, Plasma Sources Sci. Technol. **17,** 025007 (2008).
[14] J. Bohlmark, U. Helmersson, M. VanZeeland, I. Axnäs, J. Alami, and N. Brenning, Plasma Sources Sci. Technol. **13,** 654 (2004).
[15] J. Andersson, A. P. Ehiasarian, and A. Anders, Appl. Phys. Lett. **93,** 071504 (2008).
[16] A. Anders, J. Andersson, and A. Ehiasarian, J. Appl. Phys. **102,** 113303 (2007).
[17] A. Anders, J. Čapek, M. Hála, and L. Martinu, J. Phys D: Appl. Phys.**,** accepted (2011).
[18] S. M. Rossnagel and H. R. Kaufman, J. Vac. Sci. Technol. A **5,** 88 (1987).
[19] E. Ott, J. B. McBride, J. H. Orens, and J. P. Boris, Phys. Rev. Lett. **28,** 88 (1972).
[20] T. Hurtig, N. Brenning, and M. A. Raadu, Phys. Plasmas **12,** 012308 (2005).
[21] J. Lopez, Z. WeiDong, A. Freilich, A. Belkind, and K. Becker, IEEE Trans. Plasma Sci. **33,** 348 (2005).
[22] B. Liebig, N. S. J. Braithwaite, P. J. Kelly, and J. W. Bradley, Thin Solid Films **519,** 1699 (2010).
[23] A. Hecimovic, A. P. Ehiasarian, J. Winter, T. de los Arcos, R. New, V. Schulz-von der Gathen, and M. Böke, in *2nd Int. Conf. on Fundamentals and Industrial Applications of HIPIMS* (Braunschweig, Germany, 2011).
[24] W. Rasband, *ImageJ 1.44p, downloaded from http://imagej.nih.gov/ij* (National Institute of Health, 2011).
[25] A. Rauch, R. Mendelsberg, J. M. Sanders, and A. Anders, J. Appl. Phys.**,** to be submitted (2011).
[26] Y. Kudriavtsev, A. Villegas, A. Godines, and R. Asomoza, Appl. Surf. Sci. **239,** 273 (2005).
[27] E. Choueiri, Phys. Plasmas **8,** 1411 (2001).
[28] J. W. Bradley, S. Thompson, and Y. A. Gonzalvo, Plasma Sources Sci. Technol. **10,** 490 (2001).

[29] G. Buyle, W. De Bosscher, D. Depla, K. Eufinger, J. Haemers, and R. De Gryse, Vacuum **70,** 29 (2003).
[30] A. V. Phelps, "Compilation of electron cross sections, available from http://jila.colorado.edu/~avp/collision_data/electronneutral/ELECTRON.TXT," (2005).
[31] L. Spitzer Jr., *Physics of Fully Ionized Gases*, Reprint of the 2nd revised edition, originally published by Wiley, 1962 ed. (Dover, New York, 1990).
[32] L. M. Biberman, V. S. Vorobev, and I. T. Yakubov, *Kinetics of Nonequilibrium Low-Temperature Plasma (in Russ.)* (Nauka, Moscow, 1982).
[33] Y. P. Raizer, *Gas Discharge Physics* (Springer, Berlin, 1991).
[34] E. Weigold, S. T. Hood, and P. J. O. Teubner, Phys. Rev. Lett. **30,** 475 (1973).
[35] V. G. Neudachin, Y. V. Popov, and Y. F. Smirnov, Physics-Uspekhi **42,** 1017 (1999).
[36] N. Hosokawa, T. Tsukada, and H. Kitahara, in *Proc. 8th Int. Vacuum Congress* (Le Vide, Cannes, France, 1980), p. 11.
[37] W. M. Posadowski and Z. Radzimski, J. Vac. Sci. Technol. A **11,** 2980 (1993).
[38] J. Andersson and A. Anders, Appl. Phys. Lett. **92,** 221503 (2008).
[39] F. G. Tomasel, D. Carter, H. Walde, J. J. Gonzalez, and G. McDonough, Plasma Sources Sci. Technol. **12,** 139 (2003).
[40] G. Janes and R. Lowder, Phys. Fluids **9,** 1115 (1966).
[41] M. Keidar and I. I. Beilis, IEEE Trans. Plasma Sci. **34,** 804 (2006).
[42] D. Yu, C. Wang, L. Wei, C. Gao, and G. Yu, Phys. Plasmas **15,** 113503 (2008).
[43] E. Fernandez, M. K. Scharfe, C. A. Thomas, N. Gascon, and M. A. Cappelli, Phys. Plasmas **15,** 012102 (2008).
[44] D. M. Goebel and I. Katz, *Fundamentals of Electric Propulsion: Ion and Hall Thrusters* (Wiley, New York, 2008).
[45] F. Taccogna, S. Longo, M. Capitelli, and R. Schneider, Appl. Phys. Lett. **94** (2009).
[46] H. Li, F. Zhang, H. Liu, and D. Yu, Phys. Plasmas **17,** 074505 (2010).
[47] E. Chesta, C. M. Lam, N. B. Meezan, D. P. Schmidt, and M. A. Cappelli, IEEE Trans. Plasma Sci. **29,** 582 (2001).
[48] E. Y. Choueiri, Phys. Rev. E **64,** 066413 (2001).
[49] J. Kurzyna, S. Mazouffre, A. Lazurenko, L. Albarède, G. Bonhomme, K. Makowski, M. Dudeck, and Z. Peradzyński, Phys. Plasmas **12,** 123506 (2005).
[50] E. Y. Choueiri and T. M. Randolph, Phys. Plasmas **14,** 033502 (2007).
[51] A. Anders, S. Anders, and I. G. Brown, Plasma Sources Sci. Technol. **4,** 1 (1995).
[52] W. Biel, H. Kempkens, and J. Uhlenbusch, Plasma Physics and Controlled Fusion **40,** 1845 (1998).
[53] E. M. Oks, A. Anders, I. G. Brown, I. A. Soloshenko, and A. I. Shchedrin, Plasma Physics Reports **31,** 978 (2005).

Table I. Velocity of the counterclockwise, azimuthal motion of dense plasma zones observed for different gas and target material combinations. The measurement error is in the range ±50 m/s, and the given intervals refer to variations seen in the observation of several 10 measurements per gas-target combination. Atomic mass and the approximate target surface binding energies or sublimation energies (which affect the sputter yields) are also provided.[26]

target			gas		observed azimuthal velocities (m/s)
name	atomic mass (amu)	surface binding energy (eV)	name	atomic mass (amu)	
Al	30.0	3.19	Ar	39.9	8100 ± 300
Al	30.0	3.19	Kr	83.8	5400 ± 300
Cu	63.5	3.48	Ar	39.9	4200 ± 400
Cu	63.5	3.48	Kr	83.8	4200 ± 150
Nb	92.9	5.93	Ar	39.9	7000 ± 2000
Nb	92.9	5.93	Kr	83.8	5700 ± 700
W	183.4	8.7	Ar	39.9	6250 ± 300
W	183.4	8.7	Kr	83.8	4000 ± 300

Figure Captions

FIG. 1: Simplified schematic of the experimental setup for end-on observation by both the gated and streak camera; the cameras and the beam splitter were moved to the other window for side-on observations. For equipment details see text.

FIG. 2. Magnetic field of the magnetron as measured using Hall probes positioned by computer-controlled stepper motors. The arrows indicate the direction (not strength) of the **B**-vector at each of the actual measuring points; the magnetic induction B is color-coded as indicated and interpolated between measuring points. The magnetic null can be found at a distance z = 44 mm (slightly off-axis). The magnetic field arches over the target at a radius of ± 22 mm from the center; this is the location of the racetrack, indicated by the large arrows.

FIG. 3. End-on view on a niobium target operated in HIPIMS mode pulses in 0.27 Pa of argon (750 V applied, peak current 250 A, 200 pulses per second). Each individual image was taken from a different discharge pulse, under nominally the same conditions, with a different gate time as indicated next to the image. The gate time period was set that it always ended 5 µs before the current reached its peak. The contrast is visually enhanced by false color introduced by the *imageJ* software.

FIG. 4. End-on observation of a HIPIMS pulse simultaneously using the gated and streak camera, shown in the upper and lower part of the figure, respectively. The gated image identifies 4 dense plasma regions, labeled A, B, C, and D, and the streak image shows their evolution and rotation. The gated image indicates the location of the streak observation, and the streak image shows the moment of the gated image at 42.6 µs into the pulse.

FIG. 5. Top: Gated camera image, end-on view, for Nb in Ar at 0.27 Pa, 50 µs HIPIMS pulse leading to a peak current of 125.0 A; the image was taken with 10 ns exposure, 41 µs after application of the voltage when the current reached 91 A (200 pulses per second, average power 100 W). Bottom: The same discharge pulse but recorded side-on using the streak camera; the discharge current as a function of time is laid over the streak image in a way that the time axis coincides with the time axis of the streak camera image. Due to visual blocking, as explained in the text, the streak camera recorded only the plasma corresponding to the left of the end-on gated image.

FIG. 6 Side-on streak camera images of plasma emission for 50 µs HIPIMS pulses using a niobium target in argon or krypton, as indicated in the labels. The peak current reached about 125 A. The plasma light is taken from the region around (x = 22 mm, y = 0) with the slit in the z direction; the plasma emission from the region (x = -22 mm, y = 0) is blocked from view through a ceramic rod placed on target center parallel to the slit. The insets show enlargements of interesting features: the jets emanating in z-direction start at the location of greatest plasma gradient.

FIG. 7. Top: Same as in Figs. 5 and 6 but a different pulse with the gated camera image recording the discharge in side-on view. The gated image was taken with 10 ns exposure time at the time of the current peak: the flare in the center of the gated image corresponds to the last large jet seen in the streak image.

FIG. 8 Examples of time-resolved plasma potential measurements for niobium HIPIMS discharge in 0.26 Pa argon: measurements (a) at z = 16 mm and r = 28 mm, and (b) at z = 16 mm and r = 28 mm (applied voltage 488 V for 100 μs, peak discharge current 170 A, 100 pulses per second, average power 240 W).

FIG. 9. Energy dependent cross sections for electron-argon interactions. Data from the collection of A.V. Phelps.[30]

FIG. 10. Thermalization of fast electrons by Coulomb interaction with the background electrons and ions. The secondary electrons, after having picked up about 500 eV in the sheath, slow down significantly when encountering dense plasma, where they contribute to heating of the background. The path of electrons in the energy-density space is schematically shown by the arrow from the high energy to the low energy zone. Note the many orders of magnitude in thermalization time.

FIG. 11. Enlarge detail of the 5 ns image from Fig. 3. One of the magnetic field lines is indicated, aching over the racetrack and defining the onset of a dense plasma zone that provides enhanced "stopping power" to drifting energetic electrons. The triangular shape of the zone in the counterclockwise direction may be associated with the loss of energy of electrons. The plasma formed in axial direction, originating from the strongest plasma gradient in azimuthal direction, is indicated as "trailing plasma flare". The asymmetric shape of the dense plasma zone, here in end-on view, is also seen in the side-on images of Figs. 6 and 7.

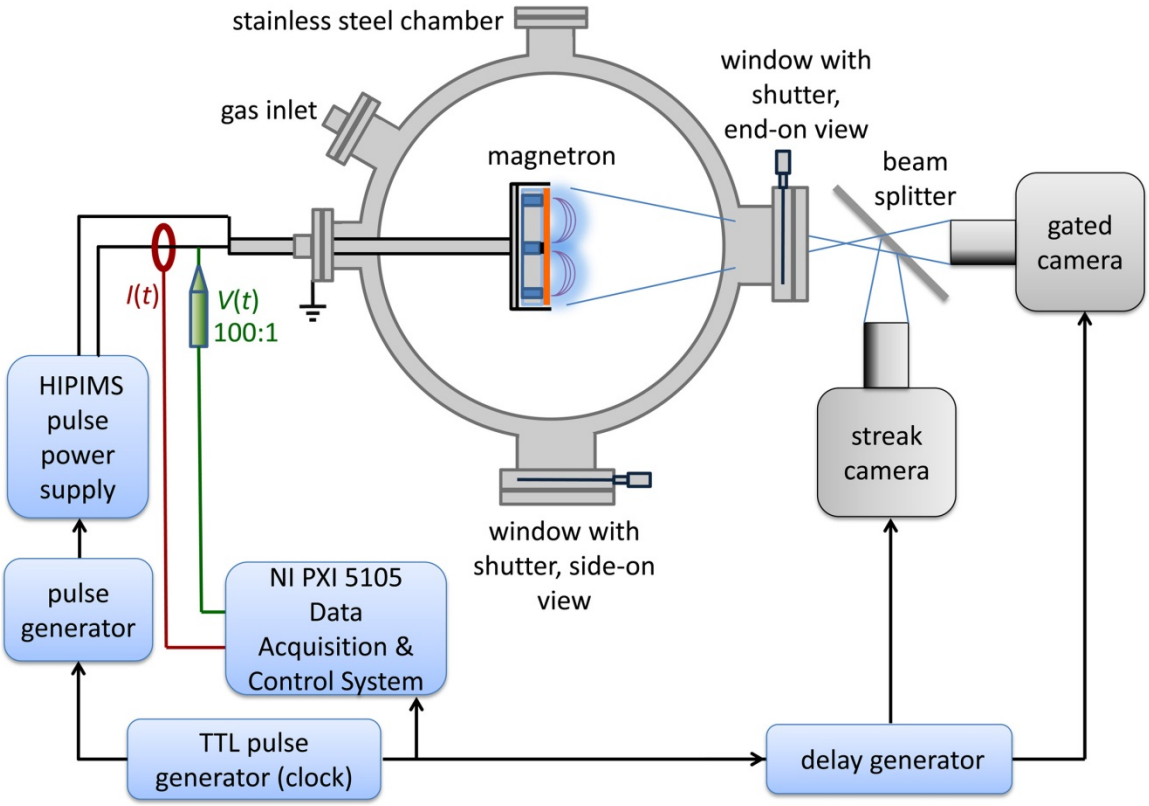
stainless steel chamber
gas inlet
window with
shutter,
end-on view
magnetron
beam
splitter
gated
camera
I(t)
V(t)
100:1
HIPIMS
pulse
power
supply
streak
camera
window with
shutter, side-on
view
pulse
generator
NI PXI 5105
Data
Acquisition &
Control System
TTL pulse
generator (clock)
delay generator

FIG. 1

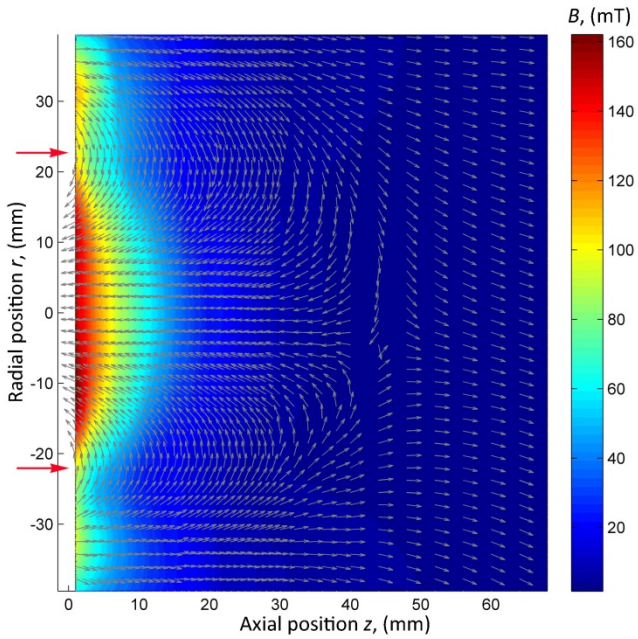
B, (mT)
160
140
120
100
80
60
40
20
30
20
10
0
-10
-20
-30
Radial position r, (mm)
0
10
20
30
40
50
60
Axial position z, (mm)

FIG. 2

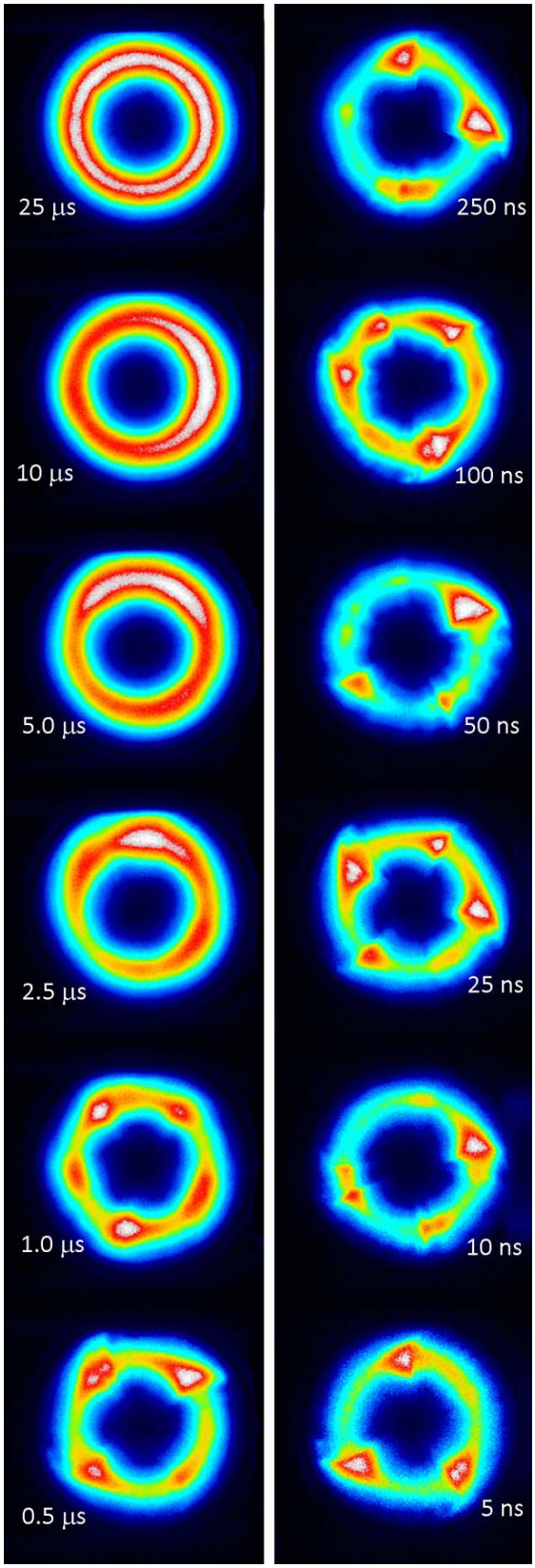

FIG. 3

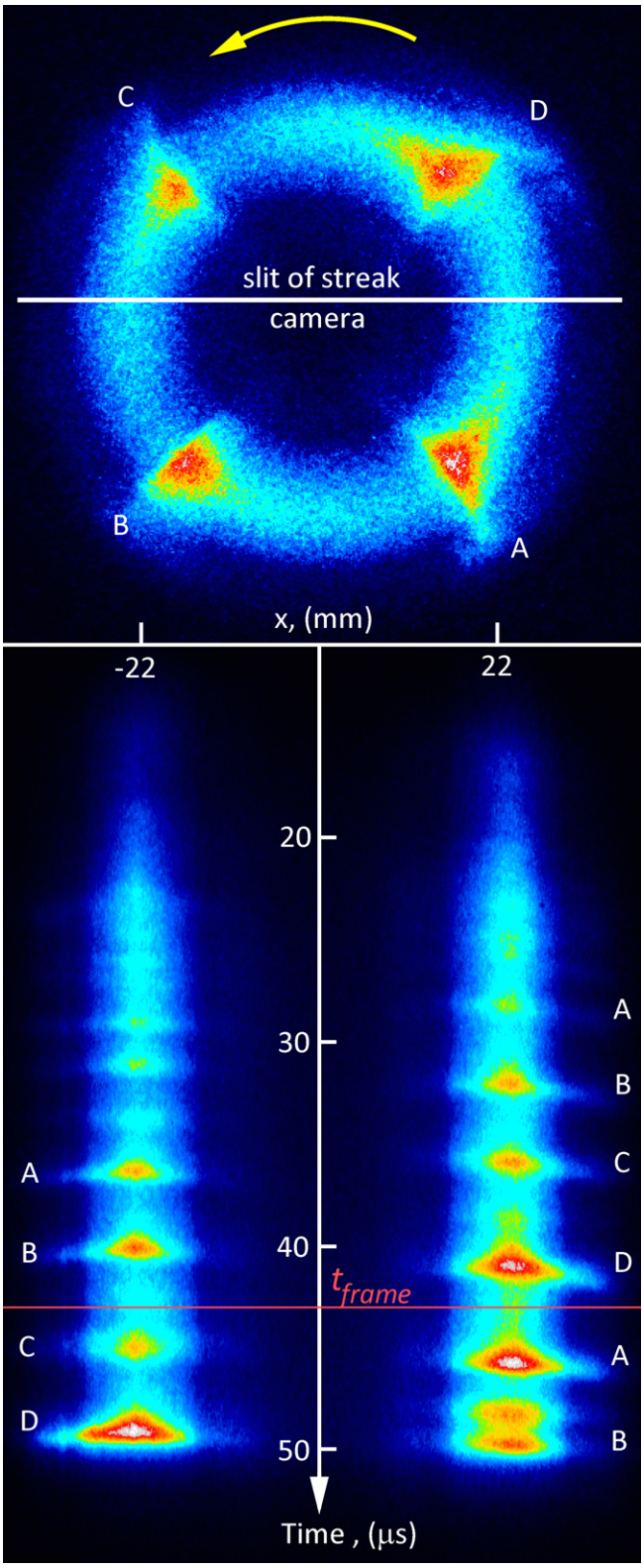
C
D
slit of streak
camera
B
A
x, (mm)
-22
22
20
30
40
50
A
B
C
D
t_{frame}
A
B
C
D
A
B
Time , (μs)

FIG. 4

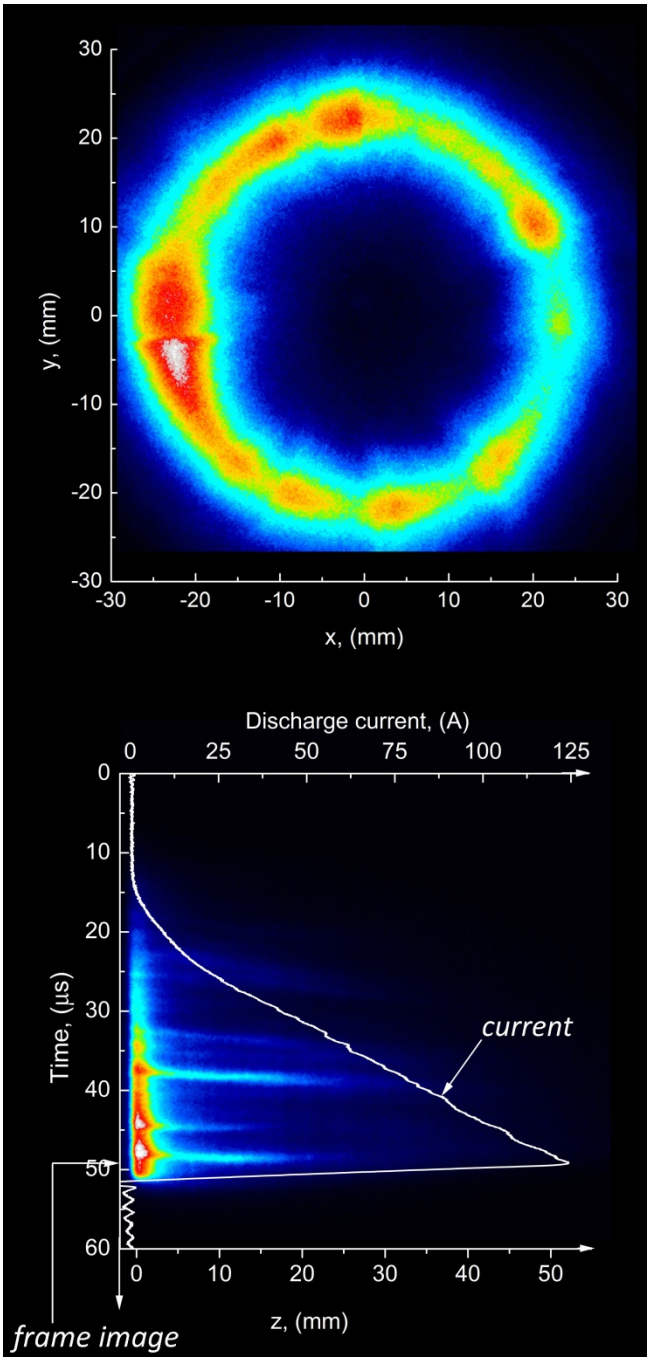

FIG. 5

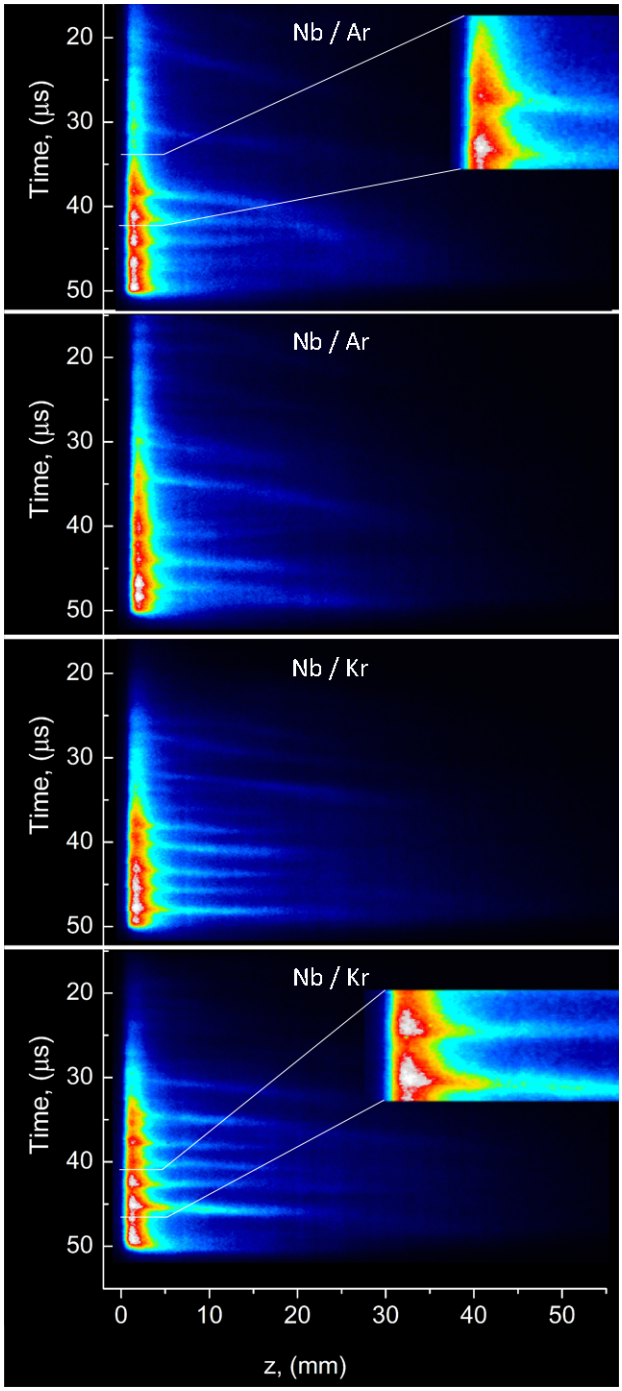

FIG. 6

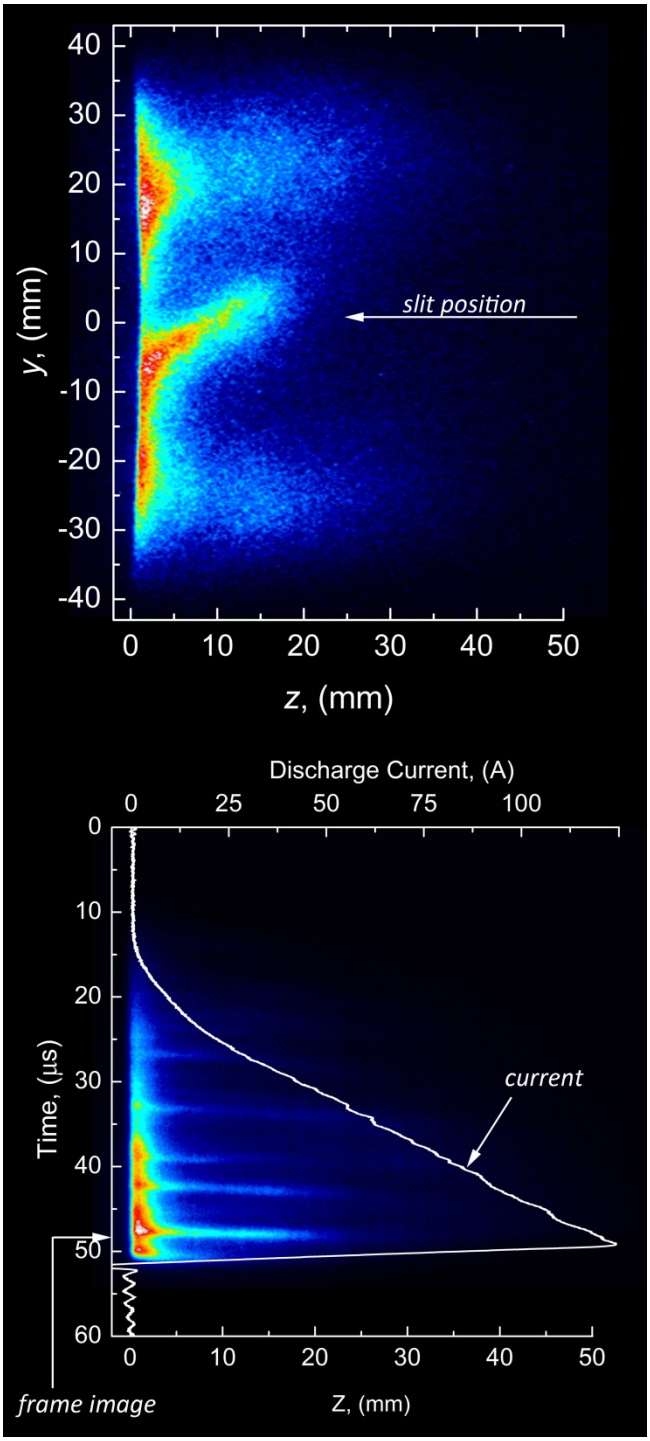
40
30
20
10
0
-10
-20
-30
-40
y, (mm)
slit position
0
10
20
30
40
50
z, (mm)
Discharge Current, (A)
0
25
50
75
100
0
10
20
30
40
50
60
Time, (μs)
current
0
10
20
30
40
50
frame image
Z, (mm)

FIG. 7

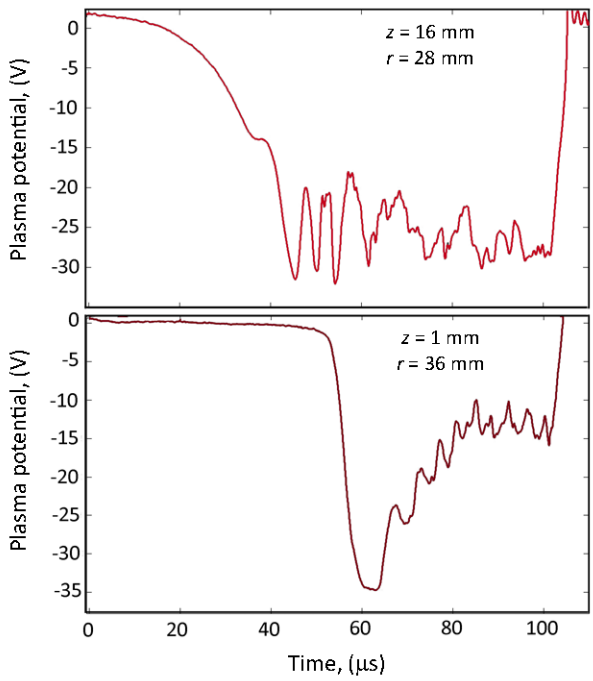
z = 16 mm
r = 28 mm
z = 1 mm
r = 36 mm
Plasma potential, (V)
Plasma potential, (V)
Time, (μs)
0
-5
-10
-15
-20
-25
-30
-35
0
20
40
60
80
100

FIG. 8

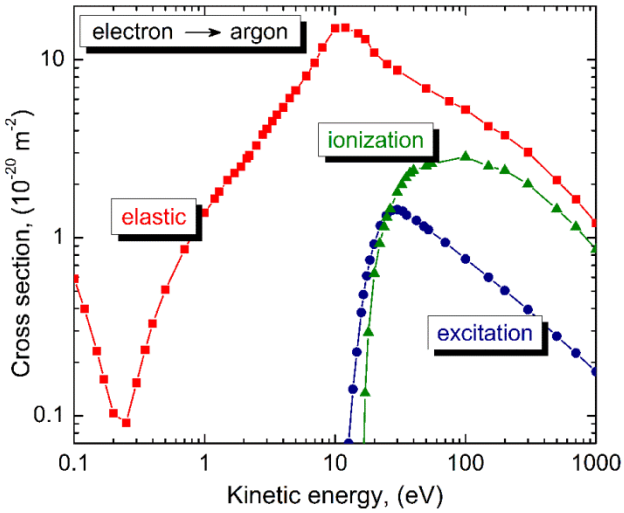
electron → argon
elastic
ionization
excitation
Cross section, (10^{-20} m^{-2})
Kinetic energy, (eV)
10
1
0.1
0.1
1
10
100
1000

FIG. 9

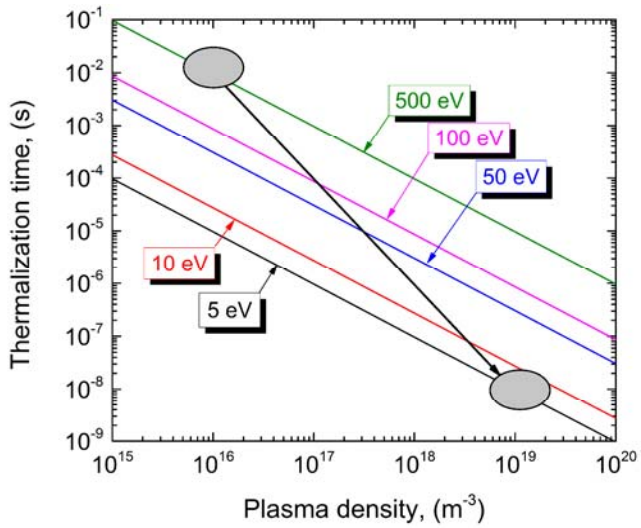
Thermalization time, (s)
Plasma density, (m^{-3})
500 eV
100 eV
50 eV
10 eV
5 eV
10^{-1}
10^{-2}
10^{-3}
10^{-4}
10^{-5}
10^{-6}
10^{-7}
10^{-8}
10^{-9}
10^{15}
10^{16}
10^{17}
10^{18}
10^{19}
10^{20}

FIG. 10

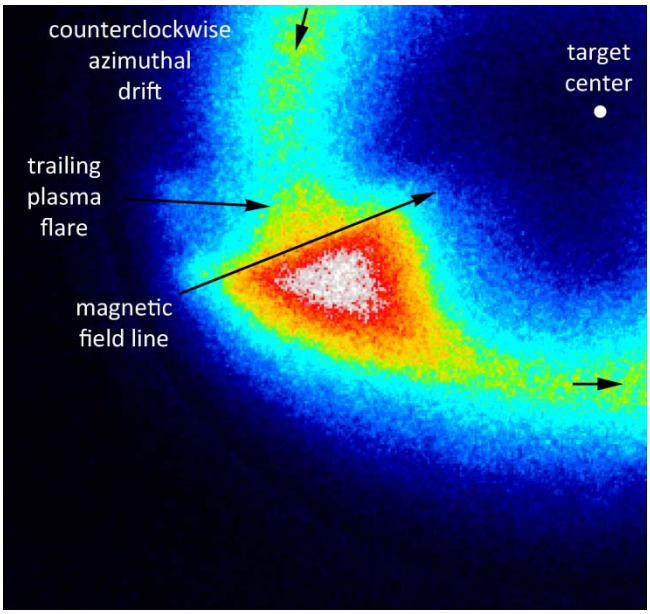
counterclockwise
azimuthal
drift
target
center
trailing
plasma
flare
magnetic
field line

FIG. 11